JOURNAL OF AIRCRAFT
Vol. 45, No. 1, January–February 2008

Investigation of a Half-Model High-Lift Configuration in a Wind Tunnel

Peter Eliasson*
FOI, Swedish Defence Research Agency, 164 90 Stockholm, Sweden

DOI: 10.2514/1.34054

An investigation is carried out for a half-model high-lift configuration inside the European Transonic Wind Tunnel. The influence of the wind-tunnel walls and model installation is investigated and the numerical results are compared with measured data and free-flight computational fluid dynamics results. The investigated model is a three-element takeoff configuration with full-span slat and flap. A computational fluid dynamics solver for unstructured grids is used for the calculations. The computed results in the wind tunnel are in good agreement with uncorrected experimental data, with maximum lift predicted at the same angle of attack. Corrected experimental and numerical tunnel data, however, deviate slightly from numerical results in free flight, for which approximately 10% higher drag is predicted. In addition, the free-flight maximum lift is predicted at a higher incidence. The lower drag in the in-tunnel results is due to a lower pressure at the leading edges of the slat and main wing close to the fuselage. This is a consequence of the current mounting of the wind-tunnel model in the tunnel, which causes a redistribution of the velocity field due to crossflow velocity components in the plane of symmetry of the half-model.

I. Introduction

CALCULATING viscous fluid flows over high-lift configurations is still a challenge in computational fluid dynamics (CFD). The difficulties in simulating these flows come from the complexity of both the geometry and flow physics. In particular, the multiple elements with small gaps give rise to multiple wakes, flow separation, laminar/turbulent transition, shock/boundary-layer interaction, etc., in which many of these phenomena interact with each other. Because the fluid dynamics is dominated by viscous phenomena, only high-fidelity simulations based on the Navier–Stokes equations can provide the required accuracy to obtain realistic CFD solutions.

The numerical simulation of the flowfield around high-lift configurations based on the Reynolds-averaged Navier–Stokes (RANS) equations has made significant progress during the last decade [1]. Until the beginning of the EUROLIFT project in early 2000, most of the European high-lift activities had been devoted to two-dimensional computations [2]. The need for an extension to three dimensions, as well as a state-of-the-art experimental database, stimulated the launch of the EUROLIFT program that was funded by the European Commission as part of the Fifth European Framework program. A close coupling and harmonization between experimental and numerical activities was attempted in the project. CFD was brought into a more daily use in EUROLIFT and introduced in three dimensions. Mainly through hybrid Navier–Stokes technology, it has become possible to compute viscous flows about takeoff and landing configurations within a reasonable time frame and with sufficient reliability. The work carried out in the EUROLIFT project has resulted in several publications; an overview is given in [3–6].

EUROLIFT II is a European High Lift Programme in the Sixth European Framework (contract AST3-CT-2004-502896), following the work initialized in EUROLIFT. The numerical and experimental investigations in EUROLIFT left many important questions unanswered, being pursued in EUROLIFT II. The investigation described here is concerned with the installation effects inside the cryogenic European Transonic Wind Tunnel (ETW), in which experiments at high Reynolds numbers are conducted. In particular, the influence of the wind-tunnel walls and model installation is investigated by conducting CFD calculations inside the wind tunnel in comparison with measurements and with computational results from free-flight calculations. Numerous CFD calculations in free flight were carried out with comparisons with experimental results from the ETW, in which reasonable agreement is reached in lift between numerical results and experiments. The maximum lift, however, is often predicted too late at a higher angle and, in particular, the drag is almost always overpredicted. This investigation was conducted to establish if this discrepancy is due to the influence from the tunnel effects and, if so, the gap between experimental and numerical results can be explained.

The considered configuration in the investigation is a simplified-takeoff wing–fuselage configuration with a full-span slat and flap. The configuration was experimentally investigated [7] during 2002 at several Reynolds numbers and loads. The same model was tested in the low-speed wind tunnel (LSWT) in Bremen at a low Reynolds number and in the cryogenic ETW in Cologne at several Reynolds numbers. The present study deals with the Reynolds number of $Re = 15 \times 10^6$, being the highest in the test campaign in the ETW. All measurements in all wind tunnels in the EUROLIFT programs were conducted with closed slots: that is, solid walls are considered in the wind tunnel.

Because high-lift configurations generate larger lift than cruise configurations at much higher angles of attack, the wall-interference corrections for wind-tunnel experimental data applied to high-lift configurations can be large. It is well known that the wind-tunnel walls may have an important effect on the fluid flow [8–10], and the current investigation aims at quantifying this influence in terms of forces, pressure distributions, and lift breakdown. Another purpose is to see how accurate the experimental wind-tunnel corrections are for high-lift flows (i.e., how well experimental results can be corrected and translated to free-flight conditions). CFD calculations inside the ETW have been carried out to investigate the slot flow in the ETW [11]. A CFD investigation [12] on wing-tip devices has shown that there are effects from the wind-tunnel walls and the mounting of a half-model for high-speed flows in the transonic regime. In the present investigation at low speed, the flow is analyzed in detail to understand the differences between the computed flowfields inside the wind tunnel and in free flight.

The numerical investigation is carried out by making computations for three angles of attack inside the ETW wind tunnel,

Presented as Paper 262 at the AIAA Applied Aerodynamics Conference, Reno, NV, 6–9 January 2007; received 15 August 2007; revision received 13 September 2007; accepted for publication 16 September 2007.

*Deputy Research Directory, Department of Computational Physics, Stockholm.

in which separate hybrid unstructured grids are generated for each angle of attack. These results are compared with uncorrected wind-tunnel data. The numerical results are then corrected to free-flight conditions and compared with free-flight numerical results at several angles of attacks and to corrected wind-tunnel data.

In the following sections, details about the geometry and the ETW wind tunnel are presented. After this follow presentations of the CFD approach, the computational grids, and the computational approach for the in-tunnel calculations. The computed results in the wind tunnel are then presented, followed by a comparison between corrected data and numerical free-flight results.

II. ETW Wind Tunnel and Model

The ETW facility is a high-Reynolds-number transonic wind tunnel using nitrogen as the test gas. High Reynolds numbers are achieved under the combined effect of low temperature and high pressure. ETW has a closed aerodynamic circuit with a Mach number range from $M = 0.15$ to 1.3. The test section is 2.0 m high, 2.4 m wide, and 8.73 m long. Downstream of 6.1 m, the test section starts increasing in cross-sectional area to reduce the flow speed. The test section is equipped with removable inserts that can be selected to yield slotted walls or solid walls, depending on the application. For half-model testing, the top wall is always closed by design and it is on this wall that the model is mounted. The slots on the floor are normally closed for half-model testing. The slots on the two side walls can be opened to reduce blockage, but were closed in the test series presented here. It was agreed within all wind-tunnel tests in EUROLIFT, for the sake of interfacility comparison, to select a test section with four solid walls, hence allowing application of an identical methodology for wall-interference corrections.

The wind-tunnel model, denoted KH3Y, is a half-model designed and manufactured by DLR, German Aerospace Research Center for use over a range of Reynolds and Mach numbers. The model is equipped with adjustable slats and flaps to enable representation of different high-lift configurations. It consists of a fuselage and a wing with full-span slat and flap. The slat and flap are positioned to correspond to a takeoff configuration. The model is mounted on the top wall (ceiling) of the ETW at a distance (peniche) to avoid the influence from the boundary layer of the wind-tunnel top wall. Figure 1 displays the KH3Y half-model high-lift configuration (shown here with a nacelle) mounted in the wind tunnel. The model has a wing span of 1.4 m and is approximately 3 m long. The peniche has the shape of the fuselage on which it is attached and keeps the same shape to the wall. Its height is 86 mm. In Fig. 1, parts of the centerbody behind the model can be seen as well. The centerbody is the downstream extension of the sector. It divides the rectangular duct in two halves and allows forming a sonic throat for Mach numbers between 0.6 and 0.95. This is achieved by setting the hinged side-wall elements and deploying the trim flaps housed in the centerbody. The setting capability can also be used as drag generator in classical tunnel operation mode to improve the stability of the tunnel set point. There, the drag rise associated with a continuous pitch-up of a model can be compensated by a simultaneous reduction of the artificially generated drag of this system. The centerbody is included in the computational domain, as subsequently described.

The model was tested in the ETW at several flow conditions. The current investigation is carried out at a Mach number of approximately 0.176 and Reynolds number of $Re = 15 \times 10^6$ based on the mean aerodynamic chord. This was the highest Reynolds number generated during the test campaign, due to stress limitations on model components, although higher Reynolds numbers can be achieved by increasing the pressure simultaneously to the temperature reduction. The temperature during this test is only 114 K. Measured quantities in the wind tunnel are the forces, pitching moment, and surface pressure at 10 spanwise sections on all three elements and inflow variables. In addition, wall surface pressure is measured at several stations along the test section. The surface pressure is used to determine the static pressure at the exit in the calculations, which will be subsequently explained.

A correction [13] is applied to the test data to translate the data to free-flight conditions. The main correction is applied to the angle of attack. For a solid wall test section configuration, the angle of attack inside the wind tunnel is smaller than the angle of attack in free flight. The following formula is applied to modify the angle of attack:

$$\Delta\alpha = \delta(1 - 2\varepsilon) \times F/F_K \times C_L^+ \tag{1}$$

where $\Delta\alpha$ is the correction to the angle of attack; δ and ε are two model dependent constants; F and F_K are the model reference area and tunnel virtual cross section area, respectively; and C_L^+ is the uncorrected lift coefficient. The uncorrected and corrected forces are plotted in Fig. 2. The correction to the angle of attack is between 1–1.4 deg. The change in the angle of attack due to the correction has a direct influence on the forces because, when translating the uncorrected in-tunnel forces to free-flight forces, the in-tunnel forces have to be projected with the corrected angle to obtain the corresponding free-flight forces. In Fig. 2, the three computed angles of attack inside the ETW tunnel are displayed as well. One angle is in

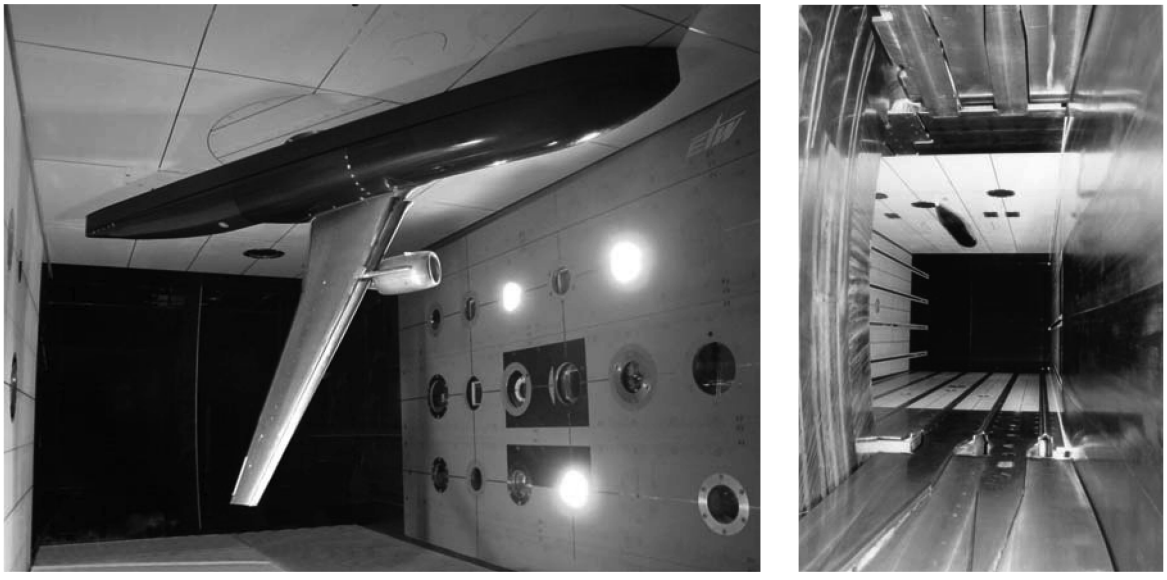

a) b)

Fig. 1 ETW test section: a) the KH3Y half-model high-lift configuration mounted in the ceiling and b) view from behind without a model mounted.

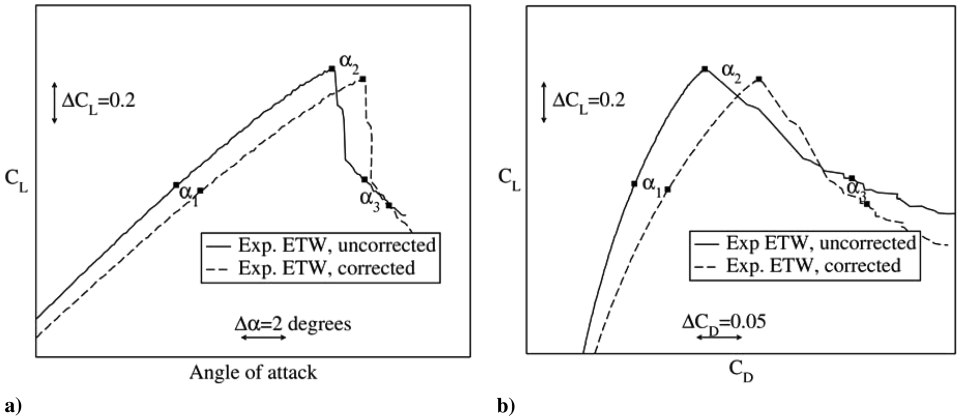

Fig. 2 Uncorrected/corrected experimental forces from the ETW: a) C_L vs α and b) C_L vs C_D; the three computed angles of attack inside the ETW are marked as α_1 in the linear range, α_2 at maximum lift, and α_3 beyond maximum lift.

the linear range α_1, and the two other angles are selected in the maximum-lift region (α_2 at maximum lift and α_3 beyond maximum lift). It was agreed within the EUROLIFT consortium to not show absolute values of forces, angles, and pressure; hence, only changes of these values are given.

In addition to the correction of the angle of attack, there are minor corrections to most variables such as the forces, moment, velocity, static and dynamic pressure, and temperature. These corrections are small (in general, less than 1%). The tunnel total states (i.e., total temperature and pressure) remain unchanged.

III. Computational Setup

A. Computational Domain Inside the ETW

To make calculations inside the ETW wind tunnel, it is necessary to make simplifications of a few details of the geometry. The simplification involves, in particular, the wind-tunnel floor and other parts of the tunnel downstream of the test section. All changes were proposed by the ETW with the intention of simplifying the grid generation with constraints, not to change the blockage of the wind tunnel. Figure 3 displays a sketch of the computational domain inside the ETW, as well as the applied coordinate system.

The incoming flow is parallel to the x axis; the angle of attack is adjusted by rotating the model around an axis parallel to the z axis. The model is mounted on the peniche attached to the top wall ceiling, which is a horizontal plane at constant z. The test section area increases slightly downstream, because the bottom wall (floor) has a small diverging angle. The computational domain includes the test section with the wind-tunnel model, and the centerbody behind the test section is also included. The motivation for this extension is hoped to have a rather uniform flow at the exit of the computational domain to prescribe a constant static pressure as a boundary condition in the computations. In addition to this extension, the upstream part is extended slightly to allow the boundary layer to develop along the tunnel walls. The complete computational domain is 13.5 m long.

B. Grid Generation

The in-house grid generator TRITET is used for the generation of all unstructured grids [14,15]. Prismatic cells are generated in the boundary layer, in which a varying number of cells are used and generated by an advancing-front technique. Outside the boundary layer, tetrahedral cells are generated by another advancing-front technique. There are usually a few elements of pyramid type to have a transition between the prismatic and tetrahedral regions.

All grids were generated for the specified model without the flap-track fairings (FTFs), because these calculations were performed early in the project to study the influence of different components. To have a direct comparison between in-tunnel and free-flight results, the FTFs were also left out in the model inside the tunnel. The influence from these devices on the total forces is limited, though. They contribute with a small fraction to the drag.

Three grids are generated in the wind tunnel for the three angles of attack α_1–α_3, because each angle requires a different setting of the model and a different grid. Note that all wind-tunnel walls are treated as viscous: that is, no-slip boundary conditions are applied and the boundary layers are resolved with $y^+ \sim 1$. One grid is generated for the half-model in free flight. Similar resolution is used for all four grids. The total number of nodes for the in-tunnel grids is 11–12 million nodes; for the free-flight grid, it is slightly less than eight million. Data about the grids are summarized in Table 1.

Some pictures of the grid at the lowest angle of attack α [1] can be seen in Fig. 4. The grids are clustered at the leading edges, on which stretched surface triangles are used with stretching ratios up to a factor of 6. Gradual grid adaptation and grid refinement were carried out to ensure that the grids are sufficiently refined and that the grid influence is small. All grids were generated in a similar manner with very similar node distribution.

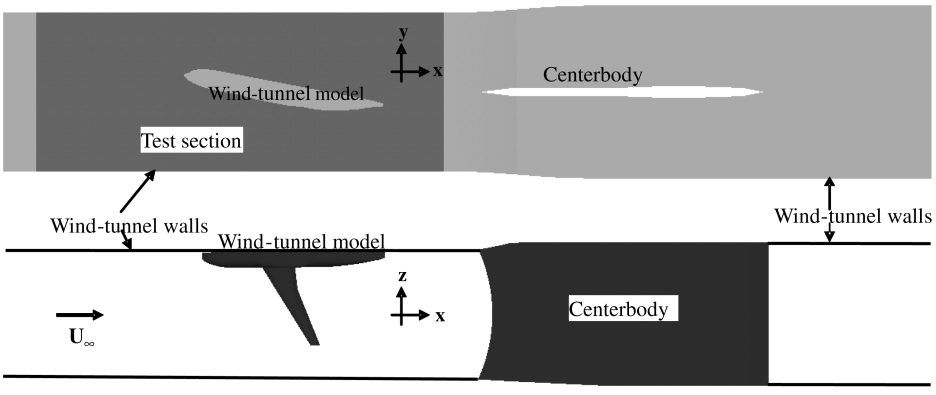

Fig. 3 Sketch of the computational domain inside the ETW: a view from above (top) and a view from the side (bottom).

Table 1 Data of the four generated grids

	Wind-tunnel grids	Free-flight grid
Total no. nodes	$11.0–11.9 \times 10^6$	7.7×10^6
Prisms	$20.3–21.9 \times 10^6$	14.1×10^6
Tetra	$4.1–5.3 \times 10^6$	2.9×10^6
Pyramids	$180–194 \times 10^6$	84×10^3
Prism layers	≤ 31	≤ 40
Boundary nodes	230×10^3	194×10^3
Boundary model nodes	200×10^3	194×10^3

C. Flow Solver

A flow solver for unstructured grids, the Edge code [16,17], is used for all CFD calculations. It is based on a finite volume approach with median dual grids. The solver adopts an edge-based formulation for arbitrary elements and uses a node-based finite volume technique to solve the governing equations. The governing equations are integrated explicitly toward steady state with Runge–Kutta time integration. The convergence is accelerated with agglomeration multigrid and implicit residual smoothing. A central spatial discretization is used for the convection of the mean flow and a second-order upwind scheme is used for the turbulence, in which the second order is enforced by a total-variation-diminishing limiter. A compact discretization of the normal derivatives of the viscous terms is used [18].

All calculations were carried out assuming fully turbulent flow due to the high Reynolds number. The turbulence model used is an explicit Reynolds stress model [19], which contains a scale-determining equation based on ω [20]. All calculations are done with a three-level Runge–Kutta scheme and four-level full-multigrid cycles, with approximately 5000 iterations to reach steady state. The boundary conditions used for the calculations in the wind tunnel are 1) no-slip wall boundary conditions at all solid walls, 2) total temperature and pressure specified at the inflow (supplied from experiments), and 3) constant static pressure at the outflow.

The calculations in free flight use no-slip wall boundary conditions, zero normal velocity in the plane of symmetry, and characteristic boundary conditions in the far field.

D. Computational Strategy in the Wind Tunnel

The computational domain in the wind tunnel was extended far downstream with the intention to have uniform outflow so that a constant static pressure can be prescribed. This pressure, however, is not known and needs to be determined. The downstream pressure completely determines the upstream Mach number and hence needs to be specified correctly. The approach taken is an iterative procedure in which the downstream pressure is varied to have a good match with available experimental tunnel wall pressure distributions. This procedure is iterated for all three computed angles of attack until a good match is obtained.

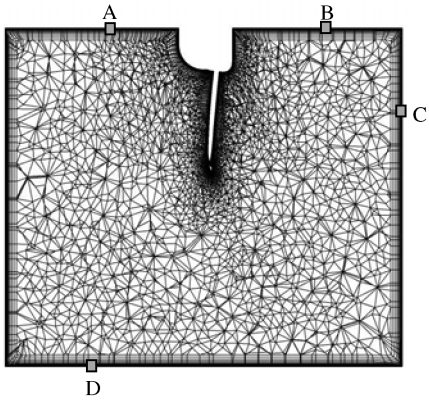

Fig. 5 Location of the four stations A–D for which wall surface pressure is available and monitored.

Four stations are chosen for which comparison between numerical and experimental wall surface pressure is carried out. Two stations (A, and B) are located at the ceiling on both the suction (A) and pressure (B) sides of the model. In addition, one station (C) on one of the side walls and one station (D) on the floor are selected. The stations are selected for which the pressure variation and influence of the model are large. All stations extend in the streamwise x direction only. The location of the stations can be seen in Fig. 5 displaying a cross section (constant x) of a cut of the grid.

In Fig. 6, wall surface pressure is plotted for two numerical solutions against experimental wall pressure. The two numerical solutions have a difference in downstream pressure of 100 Pa to show the sensitivity to the imposed downstream pressure. Note that the experimental surface pressure is only available in the test section and that the numerical results are plotted along most of the computational domain, including the test section, the rear part, and downstream extension of the wind tunnel. In the comparisons with global forces and pressure distributions, the solution with the higher backpressure is selected because it enables an excellent agreement with experimental data, as shown in Fig. 6.

IV. Results

A. Numerical Results Versus Uncorrected Data

The preceding computational procedure is repeated for the two higher angles of attack in the maximum-lift region. The calculations converge well for the two lower angles, with an approximately

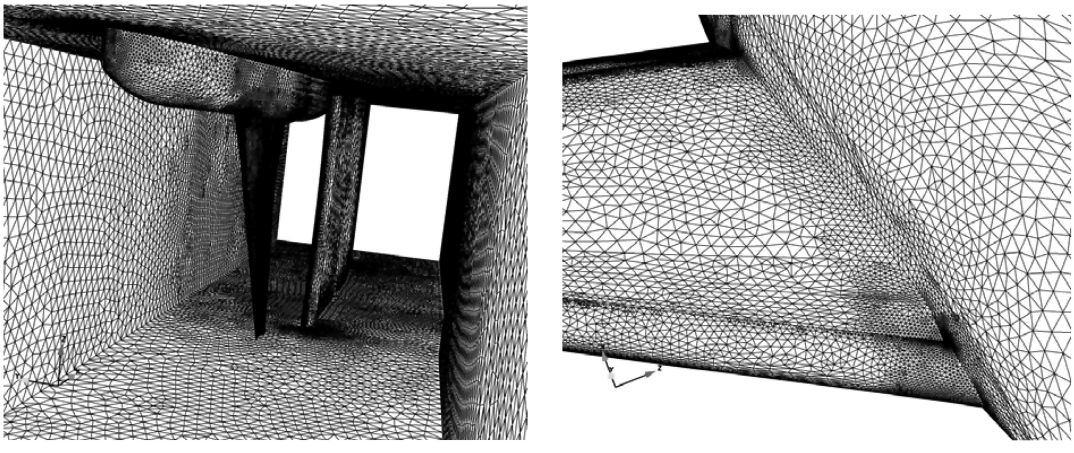

a) b)

Fig. 4 Grid pictures of the in-tunnel grid α_1: a) model mounted in the wind-tunnel ceiling with centerbody behind and b) surface grid of the wing fuselage junction.

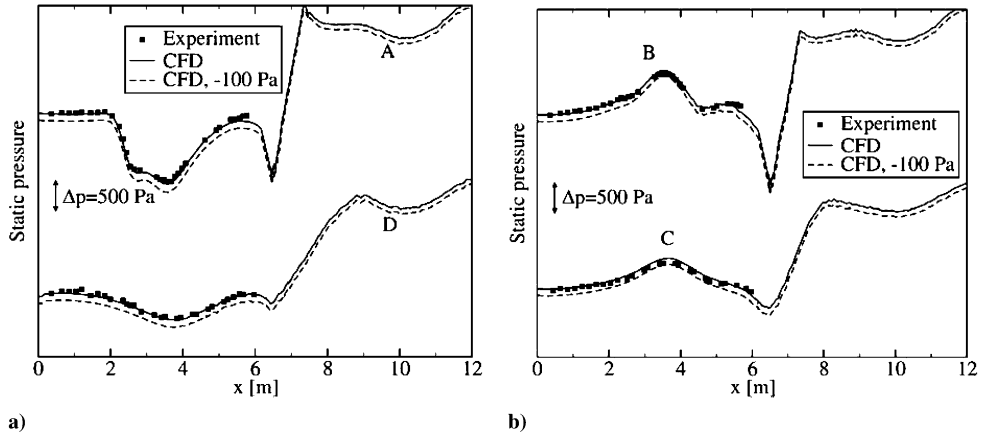

Fig. 6 Computed and measured wall surface pressure at four stations. Lowest angle of attack α_1 in linear range: a) stations A and D on the suction side of the model and b) stations B and C on the pressure side of the model. The dashed line represents a solution with 100-Pa lower backpressure compared with the solid-line solution.

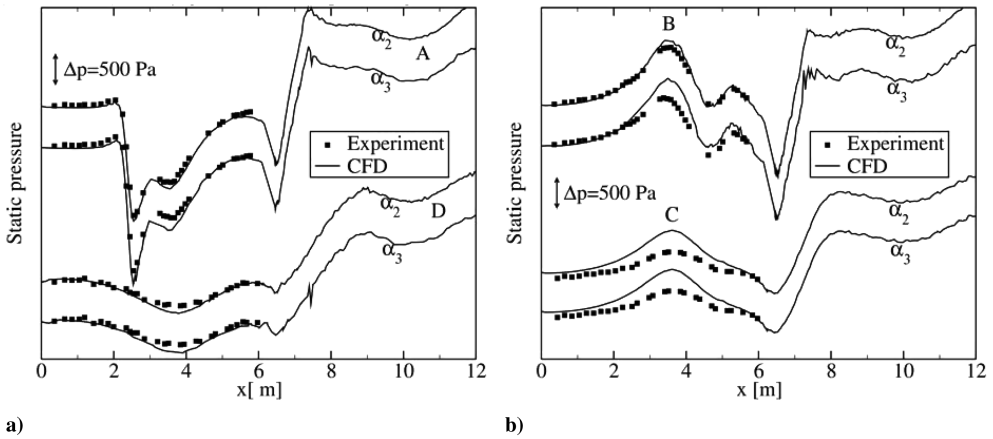

Fig. 7 Computed and experimental wall surface pressure at four stations; comparisons at the two highest angles of attack, α_2 and α_3: a) stations A and D on the suction side of the model and b) stations B and C on the pressure side of the model.

five-orders-of-magnitude reduction in the density residuals with well-converged forces. At the highest angle of attack, there are small oscillations in the forces, and a solution with average forces is used to display the following results.

The wind-tunnel wall surface pressure distributions, corresponding to Fig. 6, for the two higher angles of attack are displayed in Fig. 7. Note that the pressure curves were separated for different angles and locations A–D. This difference does not reflect a difference in pressure. As a reference, the inflow pressure is about the same at the inflow $x = 0$. The agreement between numerical and experimental data is good, but not as good as for the lowest angle in Fig. 6. The deviation between data is highest at the side wall on the pressure side (stations B and C), on which the numerical simulations predict higher pressure than measured. The agreement at the two stations on the suction side (stations A and D) is very good for all computed angles.

Figure 8 displays the Mach number at the entrance divided with the specified Mach number from experiments, which is approximately 0.175 at the lowest angle of attack. Very small deviations can be seen; the deviation is similar for the two higher angles. An integration of the Mach number over the inflow cross section gives an average Mach number that only deviates by approximately 0.2% from the tunnel-specified value. A slightly lower Mach number than specified is predicted at the right side-wall upper part, corresponding to the pressure side of the model. A slightly higher Mach number is predicted in the opposite lower left corner. Although the deviations are small, one should keep in mind that parts of the upstream variation may be due to the specification of a constant-outflow static pressure.

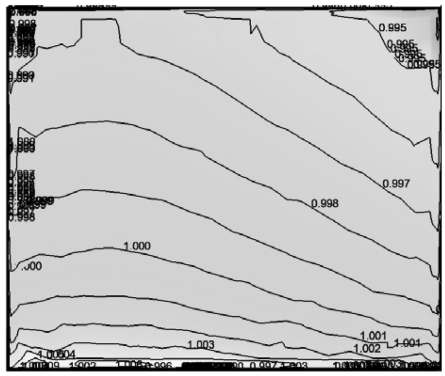

Fig. 8 Variation of Mach number at inflow; lowest angle of attack α_1, normalized with uncorrected inflow Mach number.

A comparison between the computed and experimental uncorrected forces can be seen in Fig. 9. A very good agreement is obtained. An almost-perfect match is obtained at the lowest angle of attack in the linear range. The small underprediction in drag may be due to the absence of the FTFs in the calculations. The maximum lift is predicted at the second computed angle, α_2, which also coincides with the experimental location. The level of the lift is again well-predicted for this angle; the drag is slightly underpredicted. At the highest angle of attack, the flow is about to stall, starting at the outer part of the wing. At this angle of attack, the computations show an unsteady behavior and do not converge completely to a steady state.

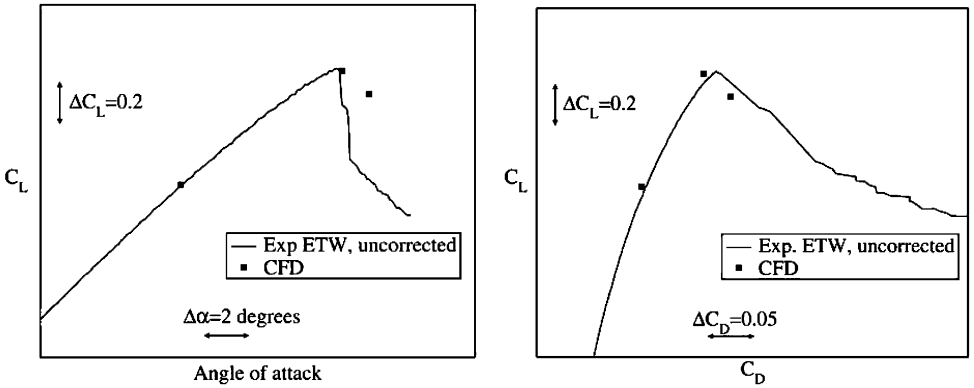

Fig. 9 Comparison between in-tunnel CFD and uncorrected experimental forces from the ETW: a) C_L vs α and b) C_L vs C_D.

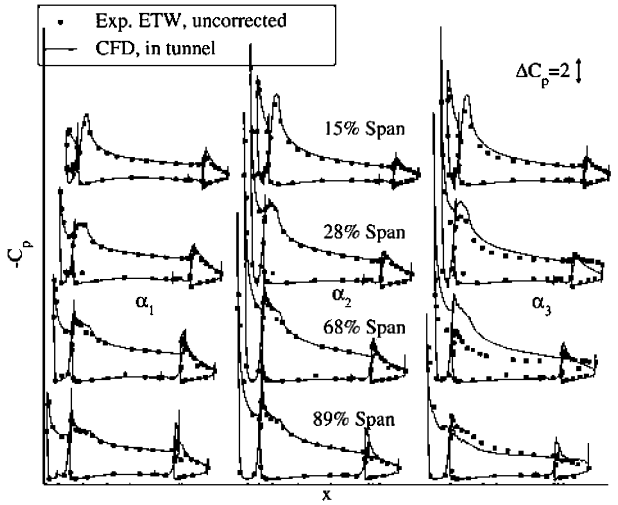

Fig. 10 Comparison the pressure distributions, uncorrected experimental values and numerical results inside the tunnel; increasing angle of attack from left to right and increasing spanwise position from top to bottom.

Average values of the forces are displayed. To improve the prediction at this angle, the correct geometry [including FTFs in combination with an unsteady RANS or hybrid RANS/LES (large-eddy-simulation) approach] should be employed.

In the pressure plots in Fig. 10, there is an excellent agreement between experimental and numerical pressure distributions at the two lower angles of attack. The lift breakdown at the highest angle of attack is clearly visible in the plot. It starts at the wing tip and propagates inboard toward the fuselage. In this case, the experimental lift breakdown reaches further inboard than predicted numerically. A separation can be observed experimentally as far inboard as at the 28% span section, but the numerical results show separation only at the most outboard station. The different extensions of separation explain the difference in the integrated forces in Fig. 9. Again, it should be emphasized that it is not expected to correctly capture the flowfield beyond maximum lift with a steady RANS calculation.

The lift breakdown is also visible in Fig. 11, in which the streamwise x component of the skin friction is plotted for the two highest angles. The plot shows that the flow is attached at the maximum lift and that the flow has started to separate on the outer part of the slat at the highest angle.

The total pressure loss distributions at five streamwise cross sections in the tunnel can be seen in Fig. 12. The first cross section intersects with the fuselage upstream of the wing. The cross sections

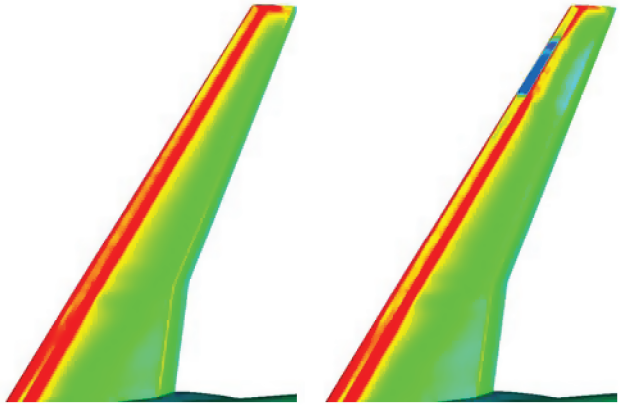

Fig. 11 Skin friction distribution (x component) inside the tunnel at the two highest angles: a) α_2 and b) α_3.

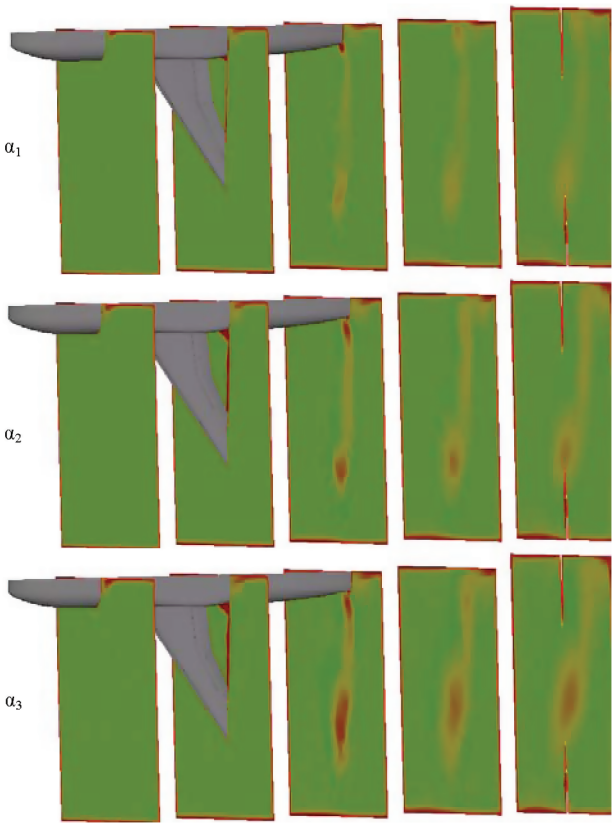

Fig. 12 Total pressure loss at five streamwise sections; the last section intersects with the centerbody.

are positioned subsequently with a constant distance of 1 m. The second cross section intersects with the wing, and the most downstream cross section intersects with the centerbody. In the plot, the tip vortex can clearly be seen traveling downstream and being amplified at higher angles of attack. The streamwise growth of the boundary-layer thickness along the tunnel walls can be seen as well. It is worth noting that the flow is attached along all wind-tunnel walls at all computed angles of attack, and hence there is no secondary flow in these regions. There is a region of higher pressure loss close to the ceiling on the pressure side of the model for all three angles. This loss is not present on the suction side. Although hard to see, there is a small separation on the leading edge of the centerbody: in particular, on the suction side close to the floor, but also on the pressure side at the ceiling. The streamwise extension of the separation is small, though, and the flow attaches shortly behind the centerbody's leading edge.

To summarize, the agreement between computed and measured data is very good up to maximum lift when comparing uncorrected experiments with in-tunnel numerical results. The next step is to compare corrected data with free-flight numerical data.

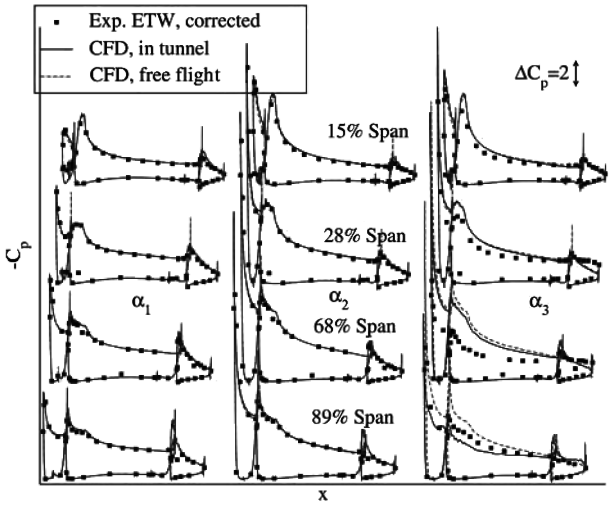

Fig. 14 Comparison of pressure distributions, corrected tunnel values and free-flight numerical results; increasing angle of attack from left to right and increasing spanwise position from top to bottom.

B. Numerical Results Versus Corrected Data

As already explained, the experimental data are corrected to correspond to free-flight conditions. This is achieved by correcting the freestream temperature, static pressure, and Mach number, due to blockage effects in the tunnel. The changes are small (in general, less than 1%). The corrected temperature and static pressure decrease, whereas the corrected Mach number increases. As a comparison, the freestream Mach number is corrected from 0.175 to 0.176 in free flight at the lowest computed angle. The main change comes from the correction of the angle of attack, which is corrected to a larger angle in the range 1–1.4 deg, as displayed in Fig. 2, and hence the lift and drag force has to be projected according to the new corrected angle of attack.

To compare the numerical results inside the wind tunnel with free-flight results, the same correction is applied to the numerical tunnel data. The velocity is scaled with the corrected Mach number and rotated with the difference between the tunnel and free-flight angle $\Delta\alpha$ according to Eq. (1). The forces are projected according to the shift in angle of attack and made nondimensional with the corrected dynamic pressure.

A comparison between computed forces from CFD and experiments is displayed in Fig. 13. A few additional angles of attack were computed in free flight.

As for the uncorrected forces in Fig. 9, there is good agreement between corrected in-tunnel CFD results and experimental values. This is a consequence of applying the same type of correction to both numerical and experimental results. The calculations in free flight, however, deviate to some extent from the data in the wind tunnel. There is a very small underprediction of lift in the linear range. The maximum lift is predicted 1 deg later in free flight, and hence the lift breakdown occurs later. The maximum-lift region is more flat and the lift breakdown occurs 1 deg later than in experiments and in-tunnel calculations. The largest deviation can be seen in the drag force. There is a shift to higher values when computing at free-flight conditions; the drag is predicted at a level approximately 10% higher than obtained when computing in the wind tunnel.

A comparison of the computed pressure distributions at the four spanwise sections for the same angles of attack as in Fig. 10 corrected to free flight can be seen in Fig. 14. The pressure coefficients in Fig. 14 were made nondimensional with the corrected dynamic pressure. The agreement between numerical results and experimental values is again very good. At first glance, the difference between the numerical results in the wind tunnel and free flight is very small. The most evident difference is that the lift breakdown at the highest angle of attack is visible in the computed pressure distribution in the tunnel at the spanwise station closest to the tip, at which the free-flight numerical results indicate attached flow. The lift breakdown results in a higher pressure on the slat and main-wing suction sides with a small streamwise variation, indicating separated flow. The pressure on the flap suction side decreases.

A closer inspection of the pressure distribution at the most inboard spanwise station in Fig. 15 reveals that the computed in-tunnel results predict a higher suction on the slat and the main wing than predicted in free flight. At the rear of the main wing (and, in particular, on the flap), a higher pressure is predicted in free flight. These differences are only visible at the most inboard station; at the next station at 28% chord, these differences have become very small.

In Fig. 16, the streamwise x component of the skin friction is displayed for the highest angle of attack, α_3, and at an angle of attack

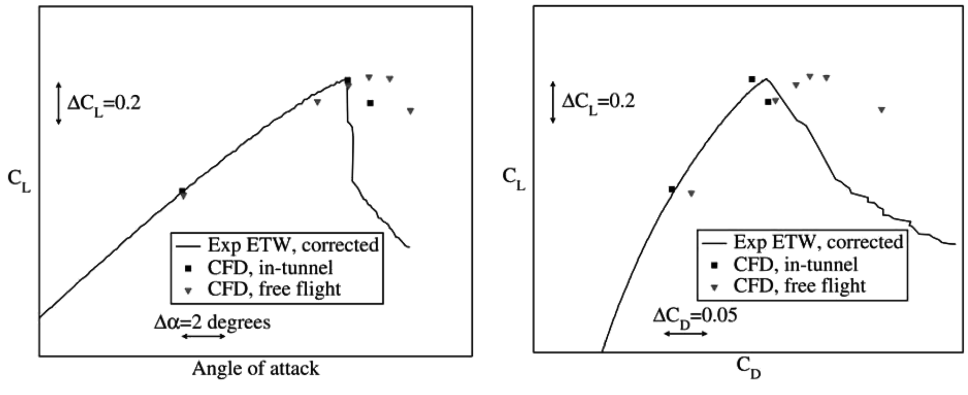

Fig. 13 Comparison of forces from free-flight CFD computations, in-tunnel CFD computations corrected to free flight, and corrected experimental forces from the ETW: a) C_L vs α and b) C_L vs C_D.

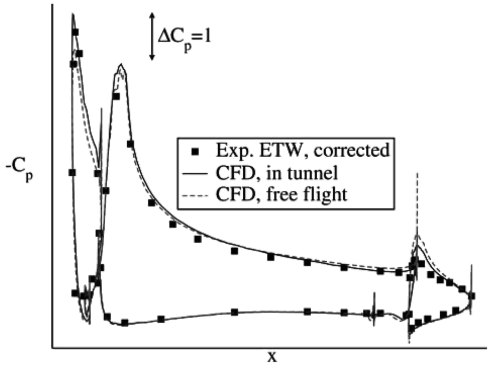

Fig. 15 Pressure distributions of tunnel results corrected to free flight; angle at maximum lift α_2; 15% span.

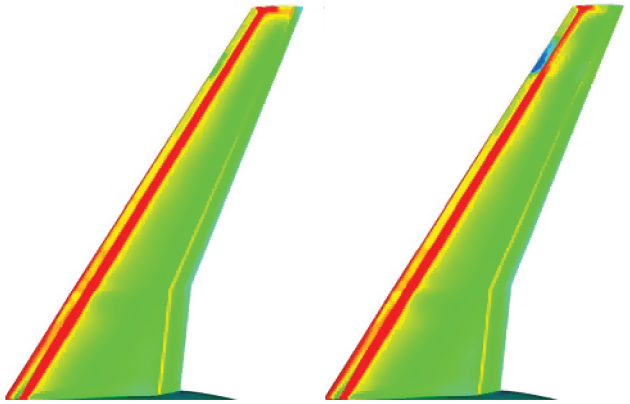

a) b)

Fig. 16 Skin friction distribution (x component) in free flight: a) α_3 and b) $\alpha_3 + 1$ deg.

of 1 deg later: $\alpha_3 + 1$ deg. The lift breakdown is caused by a separation on the slat, as obtained in the wind tunnel in Fig. 11. Hence, the lift breakdown is not affected by the model installation in the tunnel, but shifted to a higher angle in free flight.

Because the slat leading-edge pressure is lower in the in-tunnel calculations, it is likely that this is due to a higher velocity in this region. Figure 17 displays the contour of the velocity at four sections in the two calculations. A small but noticeable difference can be seen at the suction peaks, at which the velocity reaches its maximum. It is most evident at the forward section that cuts the slat only. Although hard to see, the velocity is slightly lower at the rear main wing and flap.

Another difference between the velocity contours is that there is an area with velocity gradients on the pressure side close to the wind-tunnel wall but outside the boundary layer. This region can also be traced in Fig. 12, in which a total pressure loss is detected in the same region.

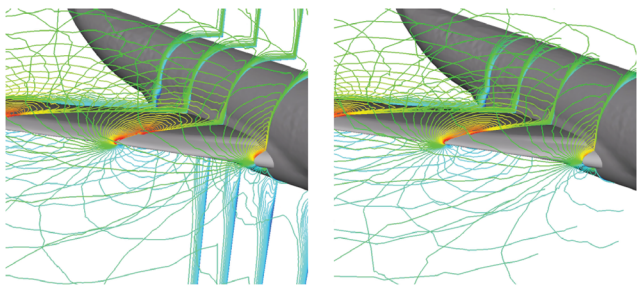

a) b)

Fig. 17 Contours of the computed absolute velocity at four stations (at streamwise x); lowest angle α_1: a) in-tunnel results and b) free-flight results.

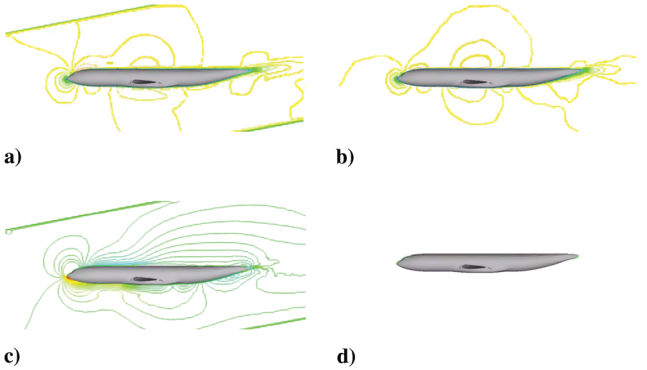

a) b) c) d)

Fig. 18 Contours of velocity in plane of symmetry; lowest angle α_1: a) in-tunnel results at streamwise x component, b) free-flight results at streamwise x component, c) in-tunnel results at crossflow z component, and d) free-flight results at crossflow z component.

The question is then why the inboard velocity distribution is different when computing in the wind tunnel than at free-flight conditions. An answer to this question is given in Fig. 18, in which the streamwise x component of the velocity and the z component of the velocity are displayed in the plane of symmetry. In the calculations in free flight, this plane is simply a plane at constant z, in which the computational domain ends and a symmetry boundary condition is applied, and in which the z component of the velocity is removed in the flux calculation. Although this is a weak boundary condition, the z component of the velocity is indeed negligible in the computed results, as can be seen.

In the wind tunnel, however, the half-model is mounted on the wall at a distance (a peniche). This distance has the same shape as the model, in that it meets the peniche and keeps the same shape to the wall. The intention with the peniche is to keep the model away from the boundary layer and to create a flowfield without crossflow velocity components in the plane in which the model and peniche meet to mimic the flow of a whole model. However, as can be seen from the velocity contours in Fig. 18, there are large crossflow z components of the velocity at this plane. In the vicinity of the stagnation point on the fuselage, there is a large positive z component of the velocity that reaches up to approximately 50% of the freestream velocity. On top of the fuselage, on the other hand, there is a rather large negative velocity component. In fact, there are significant crossflow velocity components away from the model.

These components can also be seen in Fig. 19, in which all velocity components are plotted along a line at constant y in the plane of symmetry at the approximate position at which the slat is attached to the fuselage. The maximum crossflow velocity component occurs on

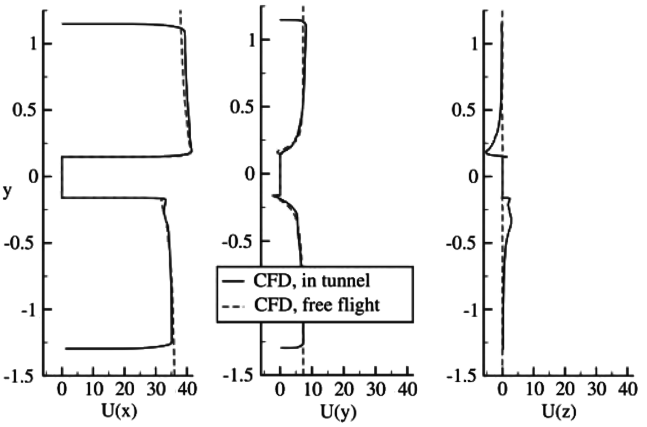

a) b) c)

Fig. 19 Velocity along y in the plane of symmetry at $x = 1$ m downstream the fuselage nose; lowest angle α_1: a) streamwise x component, b) y component, and c) z component (normal to the plane) of velocity.

the upper suction of the fuselage, corresponding to approximately 20% of the freestream velocity.

The induced crossflow velocity component hence redistributes the velocity on the inboard wing such that a higher velocity is obtained at the slat and a lower velocity is obtained at the flap. This consequently causes a lower pressure at the slat and a higher pressure on the flap. Hence, the total force vector is changed, but the size of the vector is about the same in free flight and in the tunnel. The higher inboard leading-edge velocity corresponds to a change in the local angle of attack to a higher angle in the tunnel calculations in this region. If the total force vector of the tunnel calculations is projected with an angle of approximately 0.6 deg higher than specified, a good match with the freestream lift and force is obtained.

The crossflow velocity is a result of the mounting of the model that apparently does not supply a velocity field sufficiently parallel to the plane of symmetry. It is clear that the mounting of the half-model has a potential to be improved. The size and shape of the peniche will be in focus in future studies. It is also possible that opening the side-wall slots will reduce some of the crossflow velocity.

V. Conclusions

An investigation of the influence of the wind-tunnel walls on a half-model high-lift configuration is conducted and described. The wind tunnel is the cryogenic ETW. The model investigated is the KH3Y takeoff three-element configuration with full-span slat and flap. The model is mounted in the ceiling of the wind tunnel on a so-called peniche on the wind-tunnel wall. The investigation is first carried out by conducting CFD calculations inside the wind tunnel, and numerical results are compared with uncorrected wind-tunnel experimental data. In a second step, both experimental and numerical data are corrected to correspond to free-flight conditions and further comparisons are made with CFD calculations carried out at free flight.

The Edge code for unstructured grids is used for the investigation. Three hybrid unstructured grids are generated with an in-house tool inside the wind tunnel: one grid for each computed angle of attack. In the calculations, all walls are modeled as viscous walls, for which the viscous sublayer is fully resolved with prismatic elements. The calculations in the wind tunnel are carried out by specifying a constant static pressure at the outflow of the extended computational domain, and the backpressure is adjusted to have a good match with measured pressure distribution on the tunnel walls. For the calculations in free flight, a single grid is generated with a far field and symmetry boundary for the half-model. These calculations are carried out with corrected experimental freestream data as input.

The CFD results in the wind tunnel agree very well with experimental data. There is a good match between pressure distributions and integrated forces. There is a small underprediction of the drag that is most likely due to the absence of the flap-track fairings in the numerical calculations. The maximum lift is predicted at the same angle of attack experimentally and numerically.

In the next step, the numerical results are corrected to free flight using the same wind-tunnel corrections as for the experimental data. These results, however, deviate slightly from computed numerical results in free flight. The maximum lift in free flight is predicted 1 deg later and the lift breakdown is less abrupt. The in-tunnel results predict a different velocity field in the inboard section close to the fuselage. This leads to a slightly lower pressure at the leading edge of the slat and main wing and a higher pressure at the rear main wing and flap. This corresponds to a small local change in the angle of attack and causes an overestimation of the drag force with approximately 10% in the free-flight calculations, compared with experimental and numerical in-tunnel results.

The additional velocity causing the difference in pressure is due to crossflow components in the plane of symmetry observed in the in-tunnel computed results (i.e., in the plane in which the fuselage and peniche are attached). These velocity components cause a redistribution of the inboard velocity field, pressure distribution, and forces. The fact that the flow is not parallel to this plane suggests that the mounting of the model can be improved. Opening the tunnel side-wall slots may also remove some of these crossflow components. Apart from the crossflow, there is good agreement between the in-tunnel and free-flight results. The pressure distributions agree very well from approximately 25% span out to the tip. This shows that the wind-tunnel corrections work correctly as intended.

Acknowledgments

This work was partly supported by the European Commission under contract AST-2004-502896 and carried out within the European High Lift Programme II project EUROLIFT II. The author is thankful to the European Transonic Wind Tunnel (ETW) for supplying wind-tunnel data and geometry as well as for proposing geometrical simplifications.

References

[1] Rumsey, L. R., and Ying, S. X., "Prediction of High Lift: Review of Present CFD Capability," *Progress in Aerospace Sciences*, Vol. 38, No. 2, 2002, pp. 145–180. doi:10.1016/S0376-0421(02)00003-9

[2] Lindblad, I. A. A., and De Cock, K. M. J., "CFD Prediction of Maximum Lift of a 2D High Lift Configuration," AIAA Paper 1999-3180, June 1999.

[3] Rudnik, R., "CFD Assessment for 3D High Lift Flows in the European Project EUROLIFT," AIAA Paper 2003-3794, June 2003.

[4] Eliasson, P., "CFD Improvements for High Lift Flows in the European Project EUROLIFT," AIAA Paper 2003-3795, June 2003.

[5] Perraud, J., Moens, F., and Séraudie, A., "Transition on a High Lift Swept Wing in the European Project EUROLIFT," AIAA Paper 2003-3796, June 2003.

[6] Rudnik, R., Eliasson, P., and Perraud, J., "Evaluation of CFD Methods for Transport Aircraft High Lift Systems," *The Aeronautical Journal*, Vol. 109, No. 1092, 2005, pp. 53–64.

[7] Quest, J., Wright, M. C., Hansen, H., and Mesuro, G. G., "First Measurements on an Airbus High Lift Configuration at ETW up to Flight Reynolds Number," AIAA Paper 2002-0423, Jan. 2002.

[8] Slotnick, J. P., An, M. Y., Mysko, S. J., Yeh, D. T., Rogers, S. E., Roth, K., Baker, M. D., and Nash, S. M., "Navier–Stokes Analysis of a High Wing Transport High-Lift Configuration with Externally Blown Flaps," AIAA Paper 2000-4219, Aug. 2000.

[9] Grismer, M., Kinsey, D., and Grismer, D., "Hinge Moment Predictions Using CFD," AIAA Paper 2000-4325, Aug. 2000.

[10] Rogers, S. E., Roth, K., and Nash, S., "Validation of Computed High-Lift Flows with Significant Wind-Tunnel Effects," *AIAA Journal*, Vol. 39, No. 10, 2001, pp. 1884–1892.

[11] Glazkov, S. A., Gorbushin, A. R., Ivanov, A. I., Semenov, A. V., Vlasenko, V. V., and Quest, J., "Numerical and Experimental Investigations of Slot Flow with Respect to Wind Tunnel Wall Interference Assessment," AIAA Paper 2004-2308, June 2004.

[12] Elsholz, E., and Barakat, S., "CFD Analysis of Twist Correction on Commercial Aircraft Wing with Different Tip Devices in the ETW Windtunnel," AIAA Paper 2006-513, Jan. 2006.

[13] Gross, N., and Quest, J., "The ETW Wall Interference Assessment for Full and Half Models," AIAA Paper 2004-769, Jan. 2004.

[14] Tysell, L., Berglind, T., and Eneroth, P., "Adaptive Grid Generation for 3D Unstructured Grids," *Numerical Grid Generation in Computational Field Simulation*, Mississippi State Univ., MS, 6–9 July 1998, pp. 391–400.

[15] Tysell, L., "Hybrid Grid Generation for Complex 3D Geometries," *Numerical Grid Generation in Computational Field Simulation*, Mississippi State Univ., MS, 25–28 Sept. 2000, pp. 337–346.

[16] Eliasson, P., "EDGE, a Navier–Stokes Solver for Unstructured Grids," FOI, Swedish Defence Research Agency, Rept FOI-R-0298-SE, 2001.

[17] Eliasson, P., "EDGE, a Navier–Stokes Solver for Unstructured Grids," *Finite Volumes for Complex Applications III: Problems and Perspectives*, Hermes Penton Science, London, 2002, pp. 527–534.

[18] Haselbacher, A., McGuirk, J. J., and Page, G. J., "Finite Volume Discretization Aspects for Viscous Flows on Mixed Unstructured Grids," *AIAA Journal*, Vol. 37, No. 2, Feb. 1999, pp. 177–184.

[19] Wallin, S., and Johansson, A. V., "An Explicit Algebraic Reynolds Stress Model for Incompressible and Compressible Turbulent Flows," *Journal of Fluid Mechanics*, Vol. 403, 2000, pp. 89–132. doi:10.1017/S0022112099007004

[20] Hellsten, A., "New Advanced k-ω Turbulence Model for High Lift Aerodynamics," *AIAA Journal*, Vol. 43, No. 9, 2005, pp. 1857–1869.